EFFECT OF FIR FLUXES ON CONSTRAINING PROPERTIES OF YSOS

JI-SUNG HA[1], JEONG-EUN LEE[1], AND WOONG-SEOB JEONG[2]

[1] Department of Astronomy and Space Science, Sejong University, Kunja-dong 98, Kwangjin-gu, Seoul 143-747, Korea

E-mail : uranoce27@sejong.ac.kr and jelee@sejong.ac.kr

[2] Korea Astronomy and Space Science Institute, 61-1 Whaam-dong, Yuseong-Gu, Daejeon 305-348, Korea

E-mail : jeongws@kasi.re.kr

ABSTRACT

Young Stellar Objects (YSOs) in the early evolutionary stages are very embedded, and thus they emit most of their energy at long wavelengths such as far-infrared (FIR) and submillimeter (Submm). Therefore, the FIR observational data are very important to classify the accurate evolutionary stages of these embedded YSOs, and to better constrain their physical parameters in the dust continuum modeling. We selected 28 YSOs, which were detected in the AKARI Far-Infrared Surveyor (FIS), from the Spitzer c2d legacy YSO catalogs to test the effect of FIR fluxes on the classification of their evolutionary stages and on the constraining of envelope properties, internal luminosity, and UV strength of the Interstellar Radiation Field (ISRF). According to our test, one can mis-classify the evolutionary stages of YSOs, especially the very embedded ones if the FIR fluxes are not included. In addition, the total amount of heating of YSOs can be underestimated without the FIR observational data.

Key words : stars: formation — stars: low-mass — infrared: YSOs

1. INTRODUCTION

Stars are born in their parental molecular cloud cores through gravitational contraction. After the gravitational collapse begins, a protostar with its circumstellar disk forms at the center of the collapsing core. Although the protostar/disk system is embedded in the dense infalling envelope at the early phase of evolution of star, the envelope gradually disappears as the protostar evolves to the main-sequence star. The Spectral Energy Distribution (SED) of a Young Stellar Object (YSO) is contributed by the protostar at Near-Infrared wavelengths whose temperature ranges from 2000 K to 4000 K, the disk at Mid-Infrared (MIR) wavelength which has a temperature gradient with radius, and the envelope at Far-Infrared (FIR, $40 < \lambda < 350\,\mu m$) or Submillimeter (Submm, $\lambda \geq 350\,\mu m$) wavelengths. Therefore, the analysis of the SED of a YSO can provide a way to identify the evolutionary stage of the YSO. In the SED analysis, however, we need to understand the effect of the interstellar radiation field (ISRF) since the envelope is heated by the ISRF as well as the internal source luminosity.

There is a commonly known scheme classifying the evolutionary stages of YSOs based on the shape of the SED of a YSO (Lada 1987; André et al. 1993). In this proposed scheme, the Class 0 object is in the earliest stage after the collapse begins. The Class 0 object already harbors a central heating source, but most of the mass is still in the dense envelope of gas and dust. Therefore, all emission from the central source is repro-

cessed through the envelope, which is almost isothermal with T∼30 K (Young et al. 2003).

Class I object is still heavily embedded, but emission from the central protostar and disk escapes through the outflow cavities. As a result, the peak of the SED shows at MIR wavelengths.

As the envelope material accretes to the central star through the disk and/or is cleared out by the outflows, the protostar/disk system becomes the dominant mass reservoir. Therefore, Class II objects are less embedded and have the emission excesses at near and mid-infrared wavelengths by dusty disk. The Class III objects emit energy mainly from central protostars and have only a small amount of gas in disks. The Class II and the Class III are often classified as classical T Tauri Stars and weak-line T Tauri stars, respectively (White et al. 2007).

As mentioned, in the early embedded phases, the radiation from central source undergoes the absorption/re-emission processes by the heavy envelope. As a result, significant energy is emitted at FIR wavelengths. André et al. (2000) noted that deeply embedded Class 0, whose energy peak is located at beyond 100 μm, were often missed by IRAS observations unlike the Class I objects, which reveal the peak energy emission at the wavelength from 12 to 100 μm. Therefore, the FIR data are crucial to study the evolutionary stages of embedded sources.

The envelope is also heated by the ISRF so that the SED at FIR and Submm is affected by the energy in-

put from the ISRF as well as the central source. Since the heating from the ISRF also affects the total luminosity of a YSO and the shape of the dust temperature profile, it is very important to constrain the strength of the ISRF, and thus the internal luminosity of the central heating source. The external heating by the ISRF compared to the internal heating is not negligible especially in the early embedded phase and in low luminosity sources (Dunham et al. 2008).

The AKARI/Far-Infrared Surveyor (FIS) All-Sky Survey Bright Source Catalog combined with precedented catalogs such as those by the Spitzer observations provides a useful tool to investigate the importance of the FIR fluxes in the calculations of the evolutionary indicators of YSOs, such as T_{bol} and L_{bol}/L_{smm}. In this paper, AKARI/FIS All Sky Survey Bright Source Catalog is used to investigate the importance of the FIR fluxes on the evolutionary indicators of YSOs, T_{bol} and L_{bol}/L_{smm}. In addition, we model the SED of one YSO to study how the FIR fluxes can constrain the internal luminosity and the ISRF strength around the YSO.

This paper is structured as follows. In section 2 and 3, the catalogs used in this study and the criteria adopted to select our sample YSOs are introduced. The evolutionary indicators of YSOs are summarized in section 4. We calculate those evolutionary indicators of our samples and present the results in section 5. The dust continuum modeling of the SED of one sample YSO is presented in section 6, and the summary and conclusions are followed in section 7.

2.   CATALOGS

In this study, we use various infrared point source catalogs. All of them, except for one from the observations with Spitzer Space Telescope, were obtained through the all sky survey.

2.1   InfraRed Astronomy Satellite (IRAS) Catalog

IRAS was launched on January 26, 1983 with a cooled 57 cm telescope for all-sky survey in 4 bands (12 μm, 25 μm, 60 μm, and 100 μm). The typical aperture size in each band is $3.5'$, $3.5'$, $3.6'$, and $4.7'$, respectively (Wheelock et al. 1994). Through IRAS all-sky survey, 72% of the sky was observed with three or more hours-confirming scans, and 95% was observed with two or more hours-confirming scans (Neugebauer et al. 1984).

2.2   Two Micron Sky Survey (2MASS) Catalog

Observations of the Two Micron Sky Survey began in 1997 and were accomplished in 2001 with the two telescopes located in the northern and southern hemispheres. The survey was performed for the entire sky using photometry system of 3 bands, i.e., J (1.235 μm),

H (1.662 μm), Ks (2.159 μm). The aperture size in all bands is $2.5''$(Skrutskie et al. 2006).

2.3   The c2d Spitzer legacy YSO Catalogs

The Spitzer Space Telescope (SST) was launched in 2003 which has three instruments, i.e., the Infrared Array Camera (IRAC), the Infrared Spectrograph (IRS), and the Multiband Imaging Photometer for Spitzer (MIPS). The IRAC has four bands (IRAC1, IRAC2, IRAC3, and IRAC4), which have central wavelengths at 3.6 μm, 4.5 μm, 5.8 μm, and 8.0 μm, respectively, and the beam FWHM is $1.66''$, $1.72''$, $1.88''$, and $1.98''$ in each band. Two bands of the MIPS, MIPS1 and MIPS2, have effective wavelengths at 24 μm and 70 μm, respectively, and the beam FWHM in each band is $6''$and $18''$. The YSO catalogs used for this study were provided by the Spitzer Legacy Program "From Molecular Cores to Planet Forming Disks"(c2d; Evans et al. 2003). The c2d YSO catalogs provide the IRAC and MIPS fluxes of identified YSOs in five nearby, large molecular clouds (Serpens, Lupus, Chamaeleon II, Ophiucus, and Perseus) and 58 small cores.

2.4   AKARI (ASTRO-F)/FIS Bright Source Catalog

AKARI, launched on February 2004, is a cooled 67 cm telescope with two focal plane instruments : the Far Infrared Surveyor (FIS) and the Infrared Camera (IRC). AKARI/FIS observed around 94% of the whole sky twice or more with a higher spatial resolution and a wider wavelength coverage than those of the previous all-sky mission, IRAS (Kawada et al. 2007). Due to the higher resolution of AKARI/FIS observations, AKARI/FIS could resolve the background and the source more effectively than IRAS (Jeong et al. 2007). The FIS performed the all-sky survey with 4 photometric bands (N60, WIDE-S, WIDE-L, and N160) which have an effective wavelength at 65 μm, 90 μm, 140 μm, and 160 μm, respectively. The beam FWHM of each band is $37''$, $39''$, $58''$, and $61''$, respectively (Kawada et al. 2007).

3.   DATA CRITERIA

The sample YSOs selected for this study satisfy three criteria: 1. They are listed in the c2d catalogs, 2. Their MIPS2 70 μm fluxes are greater than 1 Jy, and 3. They are detected by the AKARI but not by the IRAS.

We use YSOs from the c2d YSO catalogs as our study targets. Considering the sensitivity limit of the AKARI/FIS, only those YSOs with 70 μm fluxes greater than 1 Jy are used. The Key catalog for this study is the AKARI/FIS Bright Source Catalog since the goal of our study is to understand how FIR fluxes affect the properties of YSOs derived from observations. The IRAS catalog could be used to study the effect of the FIR, but we adopt the AKARI/FIS catalog

Table 1.
Properties of YSOs selected for this study

Index	c2d Region[1]	Spitzer Source Name[2]	R.A.(2000.0)	Decl.(2000.0)	AKARI Name
1	Ophiuchus	J163133.4-242737	247.891	-24.4594	1631337-242734
2	Ophiuchus	J163135.6-240129	247.899	-24.0247	1631357-240129
3	Lupus I	J153848.4-344038	234.703	-34.6759	1538486-344033
4	Perseus	J032538.8+304406	51.4102	30.7361	0325384+304410
5	Perseus	J032637.5+301528	51.6560	30.2584	0326374+301530
6	Perseus	J032834.5+310051	52.1426	31.0154	0328342+310055
7	Perseus	J032837.1+311331	52.1533	31.2267	0328368+311336
8	Perseus	J032845.3+310542	52.1875	31.0966	0328450+310548
9	Perseus	J032923.5+313330	52.3481	31.5575	0329235+313327
10	Perseus	J033121.0+304530	52.8372	30.7585	0331209+304531
11	Perseus	J033229.2+310241	53.1213	31.0448	0332291+310241
12	Perseus	J033312.8+312124	53.3031	31.3563	0333127+312123
13	Perseus	J033317.9+310932	53.3258	31.1597	0333182+310935
14	Perseus	J033327.3+310710	53.3642	31.1198	0333274+310711
15	Perseus	J034255.9+315842	55.7321	31.9785	0342557+315843
16	Serpens	J182815.3+000-243	277.063	-0.0444	1828152-000240
17	Serpens	J182858.1+001724	277.242	0.2896	1828580+001723
18	Serpens	J182906.2+003043	277.277	0.5116	1829064+003042
19	Serpens	J182932.0+011843	277.384	1.3119	1829322+011843
20	DC275.9+1.9	J094645.9-510610	146.691	-51.1028	0946457-510610
21	DC302.1+7.4	J124540.0-552522	191.417	-55.4212	1245402-552516
22	L100	J171603.2-205657	259.013	-20.9489	1716030-205656
23	L1251	J223031.9+751409	337.633	75.2351	2230318+751406
24	L723	J191753.7+191220	289.474	19.2054	1917539+191219
25	Lupus III	J160918.1-390453	242.327	-39.0816	1609184-390454
26	Lupus IV	J160044.5-415531	240.185	-41.9242	1600443-415527
27	Lupus IV	J160115.5-415235	240.315	-41.8752	1601157-415231
28	Lupus IV	J160221.6-414054	240.589	-41.6811	1602213-414052

[1] Name of the region where each source is located.

[2] All source names are preceded by the prefix "SSTc2d."

Table 2.
2MASS and Spitzer flux densities of YSOs selected for this study

Index	J(1.25 μm) mJy	H(1.65 μm) mJy	K_s(2.17 μm) mJy	IRAC1(3.6 μm) mJy	IRAC2(4.5 μm) mJy	IRAC3(5.8 μm) mJy	IRAC4(8.0 μm) mJy	MIPS1(24 μm) mJy	MIPS2(70 μm) mJy
1	323±6.84	515±27	602±13.3	620±34.8	540±29.7	489±23.7	673±33.9	1690±158	2560±246
2	1.00±0.05	19.0±0.5	137±2.65	589±32.8	957±52.7	1250±62.7	1450±81.8	3230±301	10400±983
3	2.15±0.28	3.84±0.6	6.60±0.54	3.95±0.40	2.76±0.52	9.58±0.75	42.7±3.11	114±11.2	2920±279
4	—	—	—	3.05±0.22	11.5±1.18	16.0±1.18	20.4±1.60	1790±167	31000±2900
5	0.18(−)	0.49(−)	1.19±0.08	3.62±0.23	9.27±0.46	11.1±0.54	12.0±0.56	396±36.7	4300±406
6	1.59±0.09	5.43±0.24	10.5±0.31	54.7±2.66	115±6.86	221±10.9	242±12.2	1160±109	2700±254
7	0.58(−)	1.18±0.14	10.1(−)	30.1±1.75	89.2±5.47	267±13.3	722±41.3	6860±639	53800±5020
8	0.06(−)	0.45(−)	0.72±0.10	1.22±0.06	2.73±0.13	2.67±0.13	2.69±0.13	213±19.9	1520±150
9	—	—	—	0.76±0.07	2.26±0.13	2.47±0.20	3.03±0.15	191±17.7	1150±110
10	—	—	—	0.12±0.01	0.85±0.05	0.83±0.05	0.62±0.04	14.7±1.37	3880±366
11	0.71±0.06	2.69±0.15	5.81±0.21	11.1±0.66	17.2±0.91	23.3±1.13	32.8±1.58	181±16.7	1130±109
12	22.4±0.39	88.8±1.31	167±2.77	301±16.3	435±26.9	642±31.8	1120±57.5	4040±382	3280±321
13	—	—	—	0.17±0.01	6.40±0.32	36.4±1.79	102±5.14	670±63.0	11700±1190
14	—	—	—	2.43±0.12	6.68±0.32	7.93±0.37	12.4±0.58	1570±147	5410±510
15	95.7±2.12	132±3.52	164±2.87	398±23.0	346±21.3	375±18.4	540±26.6	168±15.7	2430±2390
16	37.1(−)	36.4±1.21	95.2(−)	174±9.05	177±9.28	180±11.2	191±11.8	270±73.6	1670±169
17	82.5±1.98	120±3.41	111±2.26	52.5±2.97	36.7±2.47	31.2±1.68	28.5±1.68	9.74±0.92	1040±101
18	—	—	—	8.05±0.41	45.0±2.76	93.9±4.77	129±7.62	1320±139	7240±713
19	35.5±0.78	123±3.62	246±4.75	481±24.5	786±42.6	1140±57.5	1830±138	4370±407	5190±501
20	—	—	—	0.22±0.02	0.94±0.06	0.69±0.06	0.59±0.04	76.4±7.05	6590±615
21	—	—	—	0.13±0.01	1.10±0.05	2.04±0.12	2.39±0.11	87.7±8.09	1750±164
22	0.69±0.07	3.88±0.30	10.5±0.40	86.7±4.66	146±7.64	203±10.7	306±16.7	1140±106	2540±235
23	—	—	—	0.13±0.01	0.42±0.04	0.31±0.04	0.16±0.03	4.97±0.48	1400±131
24	—	—	—	0.37±0.02	4.58±0.24	11.5±0.55	16.3±0.79	295±27.3	9040±838
25	—	—	—	0.25±0.03	1.00±0.06	0.98±0.07	0.55±0.05	32.4±3.04	2610±252
26	263±6.29	344±9.82	305±6.19	177±9.40	141±7.04	140±6.81	213±11.2	590±55.2	1050±103
27	0.42±0.05	1.67±0.09	4.83±0.19	8.36±0.44	9.92±0.49	8.98±0.43	7.70±0.36	75.9±7.03	1220±123
28	1.63±0.10	3.36±0.18	4.66±0.21	5.10±0.30	4.87±0.25	12.6±0.62	42.1±2.03	144±13.4	1030±107

<div align="center">

Table 3.
AKARI FIS flux densities of YSOs selected for this study

</div>

Index	N60(65 μm) mJy	WIDE-S(90 μm) mJy	WIDE-L(140 μm) mJy	N160(160 μm) mJy
1	3874±209	3638±258	–[a]	–
2	12210±1140	12420±1360	14430±4470	21650±5660
3	3261±505	4603±104	5360±1720	–
4	80680±10600	133200±21000	124600±21200	217400±28800
5	4453±593	6092±420	12880±2490	10740±1110
6	3872±300	3757±320	6325±2010	10490±947
7	101400±1490	64350±11200	58090±10400	84570±885
8	–	2339±43	6789±1820	–
9	–	1758±162	7982±2490	–
10	3121±498	9190±259	20510±3760	25870±3390
11	–	2431±275	–	10070±182
12	3993±333	4712±182	–	–
13	15260±1370	25020±1530	46290±4150	57090±12500
14	4140±252	4442±133	–	–
15	6654±754	12640±1180	34980±7450	21750±3520
16	2298±158	3590±138	5456±1050	–
17	–	2574±99	9914±1890	7043±1550
18	38380±670	41090±1970	62110±12400	109600±7900
19	–	–	23600±6020	16030±4390
20	5544±652	11470±452	20810±2580	19110±2430
21	–	2777±130	9229±2700	–
22	–	4822±632	14440±4450	8270±1480
23	–	2164±101	7670±530	–
24	8573±1530	15800±582	31160±2020	34310±8050
25	–	3807±505	7356±938	–
26	–	1470±236	–	–
27	–	2146±218	6882±981	–
28	–	1542±66	–	–

[a] Fluxes of the flux density flag smaller than 2 are not considered.

since the AKARI resolved the point sources effectively due to its higher resolution (Jeong et al. 2007) and absolute calibration errors are expected to be less than 20% in all bands (Yamamura et al. 2010). In addition, most of 100 μm fluxes for YSOs matched with IRAS do not have a good flux quality. Therefore, we have used only AKARI/FIS sources with a good flux quality for our study. Besides, previous studies of those YSOs detected in AKARI but not detected in IRAS have been conducted without the FIR data. Therefore, it is meaningful to compare previous studies with our study, which includes FIR fluxes.

We carry out cross correlation with 6″ among catalogs based on the coordinates provided in the c2d YSOs catalogs considering positional uncertainties (Yamamura et al. 2010). There is little flux dependency of the position error on the current flux range of the sample. The AKARI/FIS catalog provides the flux density quality flag, which indicates whether observed flux density is reliable or not. For our study, we use only the fluxes flagged as "reliable" from "confirmed" sources

(Yamamura et al. 2010). Based on these criteria, 28 YSOs have been selected as our study sample, as listed in Table 1. The flux densities and their errors of these 28 YSOs are presented in Table 2 and 3.

4. EVOLUTIONARY INDICATORS

In order to classify the evolutionary stages of YSOs, a few evolutionary indicators have been used. We summarize them below.

4.1 Spectral Index

Since Lada & Wilking (1984) recognized that the SEDs of YSOs were falling into natural groups, Lada (1987) first codified the tripartite class system using the spectral index (α) between 2 and 20 μm:

$$\alpha = \frac{d\log(\lambda S_\lambda)}{d\log(\lambda)} \tag{1}$$

Table 4.
Physical properties of the selected 28 YSOs

| | | | $T_{bol}(K)$ | | $L_{bol}(L_\odot)$ | |
| | | | without FIR fluxes[2] | with FIR fluxes[3] | without FIR fluxes[2] | with FIR fluxes[3] |
Index	Spectral Index(α)	$L_{int}(L_\odot)$[1]	without FIR fluxes[2]	with FIR fluxes[3]	without FIR fluxes[2]	with FIR fluxes[3]
1	-0.610	3.371	1202	1143	0.763	0.804
2	0.140	12.590	452	380	0.919	1.116
3	0.580	3.814	180	119	0.110	0.199
4	2.160	35.148	76	53	3.094	12.593
5	1.090	5.488	105	75	0.490	0.894
6	0.830	3.544	307	234	0.846	1.167
7	2.350	59.015	119	85	6.997	13.863
8	1.110	2.065	114	84	0.196	0.282
9	1.510	1.588	104	67	0.158	0.360
10	0.980	4.983	56	41	0.316	0.856
11	0.400	1.562	283	145	0.191	0.435
12	0.410	4.255	496	458	2.822	3.078
13	3.330	14.064	92	61	1.211	2.973
14	1.930	6.811	114	107	0.962	1.066
15	-0.980	3.209	1015	549	1.300	2.489
16	-0.850	2.256	847	641	0.730	0.981
17	-1.920	1.445	1559	1033	0.466	0.711
18	1.700	8.957	138	64	1.199	6.191
19	0.260	6.550	546	448	4.168	5.168
20	1.660	8.199	59	47	0.798	1.640
21	1.910	2.357	76	50	0.246	0.502
22	0.670	3.346	334	240	0.710	1.037
23	0.700	1.911	56	36	0.164	0.311
24	2.150	11.036	72	53	1.200	2.552
25	1.100	3.432	60	47	0.141	0.227
26	-0.620	1.458	1492	1430	0.491	0.513
27	-0.190	1.679	232	136	0.051	0.098
28	0.920	1.432	276	323	0.059	0.048

[1] The intenal luminosity calculated from the flux at 70 μm (Dunham et al. 2008).

[2] T_{bol} and L_{bol} calculated only with the c2d data.

[3] T_{bol} and L_{bol} calculated with the c2d data combined with the AKARI/FIS data.

where λ is the wavelength and S_λ is the flux density at that wavelength. The boundaries of class system by Lada (1987) are as follows:

  I $0 < \alpha \lesssim 3$,

  II $-2 < \alpha \lesssim 0$, and

  III $-3 < \alpha \lesssim -2$.

After the tripartite class system by Lada (1987) was introduced, the class system has been improved by Wilking et al. (1989), André et al. (1993, 2000) and Greene et al. (1994) who formalized the 4-class system, as follows:

  I $0.3 \lesssim \alpha$,

  Flat $-0.3 \lesssim \alpha < 0.3$,

  II $-1.6 \lesssim \alpha < -0.3$, and

  III $\alpha < -1.6$.

Although this class system was based on the slope between 2.2 and 10 μm, they asserted that these classes showed no systematic deviations from classes based on the slopes between 2.2 and 20 μm. The c2d catalogs provide a least-squares fit to all photometry between 2 and 24 μm to determine the spectral index (α) and classify objects into the four classes defined by Greene et al. (1994) (Evans et al. 2009). We use α provided by the c2d catalogs as an evolutionary indicator of our selected YSOs.

4.2 Bolometric Temperature

Myers & Ladd (1993) suggests T_{bol} as a measure of the circumstellar obscuration and evolutionary development of a YSO. We calculate the bolometric temperature (T_{bol}), which is the temperature of a blackbody having the same mean frequency $\bar{\nu}$ as the observed con-
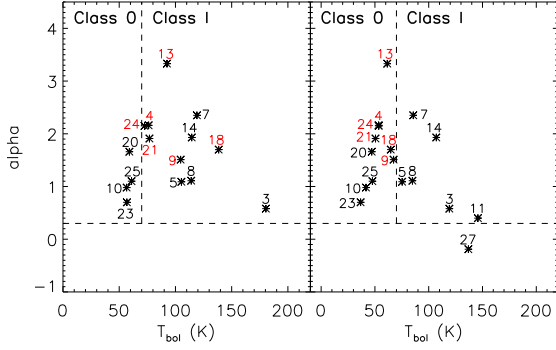
Fig. 1.— The plot of α vs. T_{bol} for a subset of the sources from Table 4. We present sources only with $T_{bol} < 200$ K in this figure. The numbers in this figure indicate the index numbers of YSOs designated in Table 1, 2, and 3. The horizontal dashed line indicates the boundary between the embedded (class 0/I) and less embedded (class II) sources, and the vertical dashed line indicates the boundary between class 0 ($T_{bol} < 70$ K) and class I (70 K $< T_{bol} <$ 650 K). The left panel shows the values of T_{bol} calculated without the AKARI FIR data, and the right panel shows those calculated with the AKARI FIR data as well. The numbers of red color denote the YSOs whose evolutionary stage changed from class I to class 0 in this comparison.

tinuum spectrum, using the prescription given in Myers & Ladd (1993),

$$T_{bol} \equiv [\zeta(4)/4\zeta(5)]h\bar{\nu}/k = 1.25 \times 10^{-11}\bar{\nu} \, KHz^{-1}, \quad (2)$$

where ζ (n) is the Riemann zeta function of argument n, h is Planck's constant, and k is Boltzmann's constant. The mean frequency $\bar{\nu}$ is the ratio of the first and zeroth frequency moments of the spectrum,

$$\bar{\nu} \equiv \frac{\int_0^\infty \nu S_\nu d\nu}{\int_0^\infty S_\nu d\nu}. \quad (3)$$

Chen et al. (1995) showed that evolutionary classes, including class 0, ranged depending on T_{bol} as follows:

0 $T_{bol} < 70$,

I $70 \lesssim T_{bol} \lesssim 650$, and

II $650 < T_{bol} \lesssim 2800$.

4.3 The ratio between L_{bol} and L_{smm}

The ratio of bolometric to submillimeter luminosity (L_{bol}/L_{smm}) can be an evolutionary indicator of YSOs, especially in the early embedded phase (André et al. 1993). L_{bol} is calculated by integrating over the full observed SED,

$$L_{bol} = \int_0^\infty 4\pi D^2 S_\nu d\nu, \quad (4)$$

while the submillimeter luminosity is calculated by integrating over the observed SED for $\lambda \geq 350$ μm,

$$L_{smm} = \int_0^{\nu=c/350\mu m} 4\pi D^2 S_\nu d\nu. \quad (5)$$

where S_ν is the flux density and D is the distance. Young & Evans (2005) suggested these boundaries for classifying protostars: $L_{bol}/L_{smm} = 35$ for Pre-Protostellar Core/Class 0, $L_{bol}/L_{smm} = 175$ for Class 0/I, and $L_{bol}/L_{smm} \sim 2000$ for the Class I/II transition.

The spectral index α is calculated without the FIR data so that it cannot be used to subdivide the embedded stage into Class 0 and Class I. However, T_{bol} and L_{bol}/L_{smm} have ability to distinguish Class 0 from Class I. A drawback to using L_{bol}/L_{smm} is in the lack of the complete data set at $\lambda \geq 350$ μm in many YSOs.

5. RESULTS

We calculated T_{bol} and L_{bol} of 28 YSOs selected by the criteria presented in section 3 in both cases of (1) only with NIR and MIR and (2) including the AKARI-FIR data as well. Table 4 lists the spectral index provided from the c2d catalogs and T_{bol} and L_{bol} calculated by integrating the observed flux density within the wavelengths covered by observations.

We calculated the internal luminosity (L_{int}) listed in Table 4 using the equation presented in Dunham et al. (2008):

$$L_{int} = 3.3 \times 10^8 F_{70}^{0.94} L_\odot, \quad (6)$$

where F_{70} is a flux density at 70 μm in cgs units (ergs $cm^{-2} \, s^{-1}$) and normalized to 140 pc. This equation is derived using the results of the linear least-square fit to the modeled L_{int} versus F_{70} in log-log space. Since F_{70} is an observable quantity, the correlation they found between F_{70} and L_{int} can be used to estimate L_{int} for sources which either lack sufficient data to constrain radiative transfer models or have such data but have not yet been modeled.

We compare the values of T_{bol} of the 28 YSOs calculated with and without the AKARI FIR fluxes in Fig. 1. According to α, 20 out of 28 YSOs are classified as Class 0/I. As mentioned, in the previous section, however, α cannot subdivide the embedded phase. Therefore, for the detail study of the early embedded YSOs, we need to use T_{bol} and L_{bol}/L_{smm}. As presented in Fig. 1, class 0 and class I objects can be divided based on T_{bol}; $T_{bol} < 70$ K for class 0 and $T_{bol} > 70$ K for class I. When the FIR fluxes are not included in the calculation of T_{bol} (the left panel of Fig. 1, see Table 4 for the whole samples), 5, 19, and 4 YSOs are classified to class II, class I, and class 0, respectively. However, when we include the FIR fluxes in the calculation of
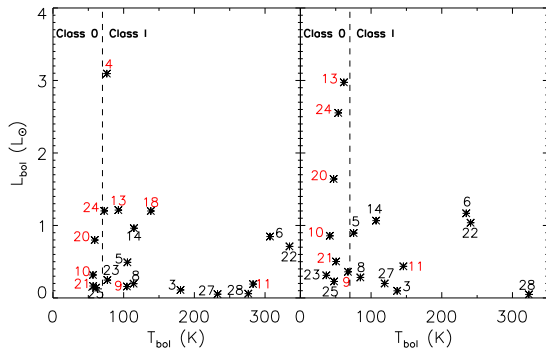
Fig. 2.— The plot of L_{bol} vs. T_{bol} for the sources from Table 4. The numbers denote the index of YSOs as listed in Table 1. The categories of two panels are the same as in Fig. 1, that is, without (left panel) and with (right panel) the FIR fluxes in the calculation of L_{bol}. The dashed line indicates the boundary between class 0 and class I in T_{bol}. The numbers of red color denote the YSOs whose L_{bol} increases more than twice when the FIR fluxes are included in the calculation of L_{bol}.

Fig. 3.— The same plot as Fig. 2 but for YSOs with higher L_{bol}. The values of L_{bol} of sources 4 and 18 increase more than 4 times when the FIR fluxes are included in the calculation of L_{bol}.

T_{bol} (the right panel of Fig. 1), 3, 15, and 10 YSOs are classified to class II, I, and 0, respectively.

That is, 6 YSOs are reclassified to class 0 from class I, and 2 YSOs are reclassified to class I from class II. As a result, YSOs detected in the FIR wavelengths are mostly (25 out of 28) embedded. This comparison shows that the FIR fluxes are very important to know the evolutionary stages of YSOs, especially for the embedded ones.

Fig. 2 and 3 present the same comparison but for L_{bol}. When the FIR fluxes are included in the calculation of L_{bol}, the values of L_{bol} of 10 YSOs increase by more than a factor of 2. Two of them (sources 4 and 18) even increase by more than a factor of 4 in their values of L_{bol}. This change in L_{bol} possibly increases the ratio, L_{bol}/L_{smm}, resulting in different evolutionary stages of the YSOs. According to our comparisons in the calculations of T_{bol} and L_{bol} with and without the FIR fluxes, we can see how important knowing the FIR fluxes of YSOs, especially the embedded ones, is.

6. ONE-DIMENSIONAL DUST RADIATIVE TRANSFER MODELING

The original radiation from the central source and circumstellar disk is scattered, absorbed and reemitted by the dusty material in the envelope. The embedded sources have thick envelopes, where most of mass resides, and which can be well described by a sphere. Therefore, in order to get the detailed information on YSOs, the emerged SED must be modeled. In this study, we modeled the SED of a YSO using a 1-D radiative transfer code to test how the FIR fluxes can constrain the physical parameters of the YSO.
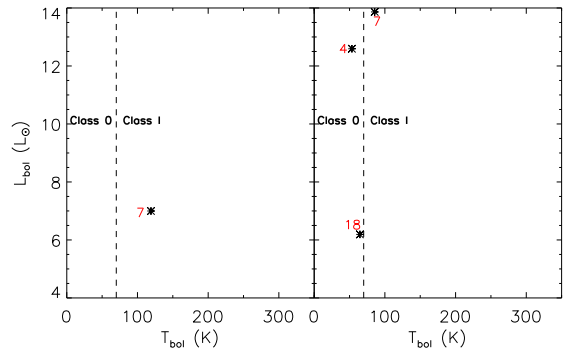
The selected YSO for this test is the source 13 in Table 1. Its Spitzer source name is J033317.9+310932, and it is located in a large molecular cloud, Perseus. As listed in Table 4, L_{bol} is ∼1.2 and ∼3.0 $L_{\odot}$ when calculated without and with the FIR fluxes, respectively. In the early embedded phase, the heating by the ISRF cannot be ignored compared to the heating by the central source (Young et al. 2003). Therefore, in order to know the accurate internal luminosity, which is a crucial quantity to understand the formation mechanism of the protostar, separately from the ISRF luminosity, we must model the observed SED.

J033317.9+310932 was not detected by the 2MASS observations. This source is listed as Bolo 80 in the Bolocam survey of Perseus for 1.1 mm dust continuum emission (Enoch et al. 2006). The observed fluxes and calculated T_{bol} and L_{bol} of this YSO are listed in Table 2, 3, and 4. We use the one-dimensional radiative transfer code, DUSTY (Ivezic et al. 1999) to model the SED of J033317.9+310932. The program, ObsSphere (Shirley et al. 2002) is then used to match the results from DUSTY with the actual observed fluxes at wavelengths longward of 100 μm. ObsSphere calculates the fluxes emerging only from the envelope, which is the dominant flux source at long wavelengths, based on the physical conditions derived from DUSTY. Refer to Dunham et al. (2006) for the detailed description of the model input parameters.

We modeled the SED with and without the FIR fluxes and compared the derived properties of the central heating source (star/disk) and the envelope. The envelope is assumed to have a power-law radial density profile [$n(r) \propto r^{-p}$]. We have tested the envelope model by changing the p parameter from 1.5 to 2.0. According to the inside-out collapse model (Shu et al. 1977), the density profile has the power of 1.5 and 2 at radii smaller and larger than the infall radius, respectively. The heating sources for our model are the internal star/disk system and the ISRF. In general, since
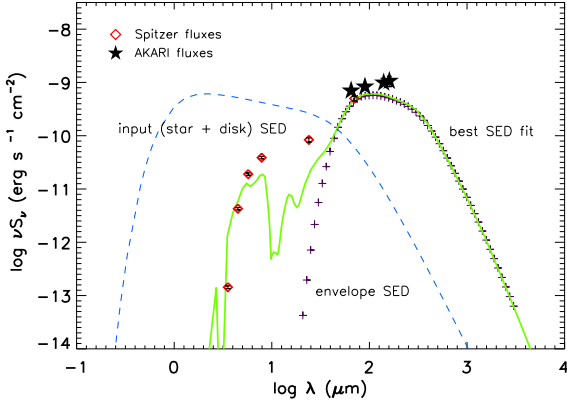
Fig. 4.— The best-fit model of the SED of J033317.9+310932 when only the Spitzer data are used. The green solid line indicates the best-fit model SED obtained by DUSTY, and red open diamonds represent the Spitzer photometry data. The blue dashed line shows the input SED for the model. The purple crosses show the emerging SED only from the envelope which is calculated with ObsSphere based on the model density profile and the temperature profile obtained from DUSTY. The star symbols denote the AKARI fluxes, which are not included for this SED model. The best-fit model only with the Spitzer fluxes does not match well the AKARI fluxes.

cores with YSOs are embedded in bigger clouds, the ISRF reaching the surface of a core is attenuated by the surrounding material. We tested various attenuator of the ISRF, which is parameterized by the visual extinction (A_V) since the UV field strength of the ISRF relative to the local ISRF, G_0 is given by $e^{-1.8A_V}$ (Lee et al. 2004).

For the dust opacity, as many studies did (Shirley et al. 2002; Young et al. 2003; Evans et al. 2005), we adopted the OH5 dust model, which is for the thin ice mantles coagulated for 10^5 years at a gas density of 10^6 cm^{-3} (Ossenkopf & Henning 1994).

To find the best-fit envelope model we calculated the reduced χ^2 (Dunham et al. 2006),

$$\chi^2 = \frac{1}{n-1} \sum_{i=0}^{n} \frac{[S_\nu^{obs}(\lambda_i) - S_\nu^{mod}(\lambda_i)]^2}{\sigma_\nu(\lambda_i)^2}, \qquad (7)$$

where $S_\nu^{obs}(\lambda_i)$ is the observed flux density at λ_i, $S_\nu^{mod}(\lambda_i)$ is the simulated flux density from this model at same wavelength, and $\sigma_\nu(\lambda_i)$ is the uncertainty in the observed flux density. And n is the number of the data points, so the model with the FIR fluxes has four more data points than the other model without the FIR fluxes for the case of J033317.9+310932.

Fig. 4 shows the best-fit model without the FIR fluxes. The model parameters of this model are listed in Table 5. The best-fit model does not match very
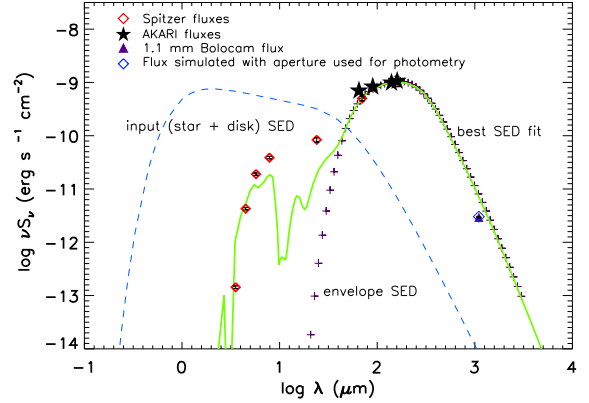

Fig. 5.— The best-fit model SED when the AKARI FIR fluxes as well as the Spitzer data are included. The purple triangle and open blue diamond indicate the observed 1.1 mm Bolocam flux and the flux simulated from the model with the aperture used for the 1.1 mm flux measurement, respectively. Other colors and symbols are the same as in Fig. 4.

well the observed 8 and 24 μm fluxes. This is possibly because the disk emission is not well modeled with our 1-D calculation. As seen in Fig. 4, this best-fit SED cannot match the AKARI fluxes. According to this best-fit model, the ISRF is completely obscured by surrounding medium, and the internal luminosity is about 3.8 $L_\odot$.

Fig. 5 presents the best-fit model when the FIR fluxes are included. The parameters of this model are also listed in Table 5. The internal luminosity increases ~25% compared to the model without the FIR fluxes, and a higher UV field strength of the ISRF is necessary to fit the AKARI fluxes. The model SED shows that the peak of the SED is located at the wavelength of ~160 μm, which is the longest wavelength of the AKARI FIS. In order to constrain the SED better, however, observations at longer wavelengths than the AKARI bands are necessary.

The density (upper panel) and temperature (lower panel) distributions of the envelope with radius for the best-fit models with (blue solid line) and without (red dashed line) the FIR fluxes are presented in Fig. 6. Since AKARI FIR fluxes listed in the catalogue are not color corrected ones, we applied color correction to AKARI FIR fluxes by using our modeled SEDs. The variation of color correction factor in our models does not exceed 10%. The envelope density profile of the best-fit model with the FIR fluxes has the power of 1.9, which is similar to the density profile of the static envelope in the Shu's inside-out collapse model. This result might indicate that J033317.9+310932 is in a very early stage of collapse, so the infall radius is still small.

The physical parameters for the best-fit model with

Table 5.
The best-fit models for the SED of J033317.9+310932

model	p[1]	R_{inner}[2]	R_{outer}[3]	M_{env}[4]	n_{1000AU}[5]	G_0[6]	L_{int}[7]	T_{star}[8]
	–	AU	AU	$M_\odot$	cm^{-3}	–	$L_\odot$	K
without FIR fluxes	1.6	650	20000	5.9	1.5×10^6	0	3.8	2800
with FIR fluxes	1.9	880	29000	7.6	2.4×10^6	0.4	4.7	3000

[1]The power of the power law envelope density profile.

[2]The inner radius of the envelope.

[3]The outer radius of the envelope.

[4]The mass of the envelope.

[5]The fiducial density at 1000 AU.

[6]The UV field strength of the ISRF relative to the local ISRF.

[7]The internal luminosity caused by the accretion to the star/disk system.
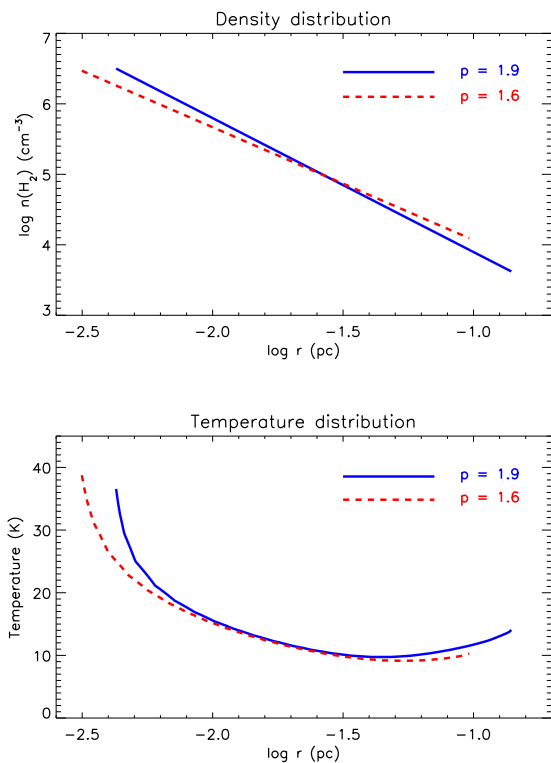
[8]The temperature of the central protostar.

Fig. 6.— The envelope physical structures obtained from the dust continuum modeling as a function of radius. The upper and lower panels present the density and temperature structures, respectively. The red dashed lines are for the best-fit model without the FIR fluxes while the blue solid lines are for the best-fit model with the FIR fluxes.

the FIR fluxes show differences from those for the best-fit model without the FIR fluxes. As mentioned above,

the power of the density profile is different in the two models. In addition, the envelope mass of the best-fit model with the FIR fluxes is about two solar mass greater than the best-fit model without the FIR fluxes. Other important parameters are the internal luminosity (L_{int}) and the UV strength of the ISRF (G_0), which are two heating sources of the envelope. According to our test, L_{int} and G_0, constrained by the SED modeling, are probably close to $L_{int} = 4.7\ L_\odot$ and $G_0 = 0.4$ rather than $L_{int} = 3.8\ L_\odot$ and $G_0 = 0$. Here, $G_0 = 0.4$ is equivalent with the UV field attenuated by $A_V = 0.5$ mag.

7. SUMMARY AND CONCLUSIONS

We tested the effect of FIR fluxes in classification of the evolutionary stages of YSOs and in calculation of the internal luminosity as well as the UV strength of the external heating source, the ISRF. Twenty eight sample YSOs, which have their counterparts only in the AKARI/FIS Bright Source Catalog, were selected from the c2d YSO catalogs. First, we calculated an evolutionary indicator, T_{bol}, and found that 6 objects, which are classified into class I when only Spitzer fluxes were used, were reclassified into class 0 when the AKARI FIR fluxes were included. Two objects, which were classified into class II when only the Spitzer data were included, were also reclassified into class I. This result shows that the FIR observations are very important in the classification of the evolutionary stages of the early embedded YSOs since they emit most of their energy at the long wavelength regime.

In order to test how the FIR fluxes constrain the physical structure of the envelope, the internal luminosity, and the UV strength of the ISRF, we modeled the SED of one of our sources. In the early evolutionary phase, the external heating by the ISRF can not be ignored compared to the internal heating.

According to our dust continuum modeling, when the FIR fluxes are included, the density profile of the envelope is steeper (p=1.9 compared to p=1.6) indicating most of envelope material is possibly static, that is, the infall radius is very small in the sense of Shu's inside-out collapse model. The estimated internal luminosity is constrained to 4.7 $L_\odot$ when the FIR fluxes are included (compared to 3.8 $L_\odot$ obtained when the FIR fluxes are not included). The UV strength of the ISRF is G_0=0.4 (attenuated by $A_V = 0.5$ mag) in the model with the FIR fluxes, but in the model without the FIR fluxes, the ISRF needs to be completely attenuated (G_0=0). Our modeling result also indicates that fluxes at FIR and even longer wavelengths are crucial to better constrain the physical parameters of embedded YSOs.

ACKNOWLEDGMENTS

REFERENCES

Andrè, P., Ward-Thompson, D., & Barsony, M. 1993, Submillimeter Continuum Observations of Rho Ophiuchi A - The Candidate Protostar VLA 1623 and Prestellar Clumps, ApJ, 406, 122A

Andrè, P., Ward-Thompson, D., & Barsony, M. 2000, From Prestellar Cores to Protostars: the Initial Conditions of Star Formation, in Protostars and Planets IV, 59

Chen, H., Myers, P. C., Lada, E. D., & Wood, D. O. C. 1995, Bolometric Temperature and Young Stars in the Taurus and Ophiuchus Complexes, ApJ, 445, 377C

Dunham, M. M., Evans, N. J. II, Bourke, T. L., Dullemond, C. Y., Young, C. H., Brooke. T. Y., Chapman. N., Myers, P. C., Porras, A., Spiesman, W., Teuben, P. J., & Wahhaj, Z. 2006, The Spitzer c2d Survey of Nearby Dense Cores. I. First Direct Detection of the Embedded Source in IRAM 04191+1522, ApJ, 651, 945

Dunham, M. M., Crapsi, A., Evans, N. J. II, Bourke, T. L., Huard, T. L., Myers, P. C., & Kauffmann, J. 2008, Identifying the Low-Luminosity Population of Embedded Protostars in the c2d Observations of Clouds and Cores, ApJS, 179, 249

Enoch, M. L., Young, K. E., Glenn, J., et al. 2006, Bolocam Survey for 1.1 mm Dust Continuum Emission in the c2d Legacy Clouds. I. Perseus, ApJ, 638, 293E

Evans, N. J. II, Allen, L. E., Blake, G. A., Boogert, A. C. A., Bourke, T., Harvey, P. M., Kessler, J. E., Koerner, D. W., Lee, C. W., Mundy, L. G, Myers, P. C., Padgett, D. L., Pontoppidan, K., Sargent, A. I., Stapelfeldt, K. R., van Dishoeck, E. F., Young, C. H., & Young, K. E. 2003, From Molecular Cores to Planet-Forming Disks: An SIRTF Legacy Program, PASP, 115, 965

Evans, N. J. II, Lee, J.-E., Rawlings, J. M. C., & Choi, M. 2005, B335: A Laboratory for Astrochemistry in a Collasing Cloud, ApJ, 626, 919

Evans, N. J. II, Harvey, P. M., Dunham, M. M., Hward, T. L., Mundy, L. G., Lai, S.-P., Chapman, N., Brooke, T. Y., & Enoch, M. L. 2007, Final Delivery of Data from the c2d Legacy Project: IRAC and MIPS

Evans, N. J. II, Dunham, M. M., Jorgensen, J. K., Enoch, M. L., Merín, B., van Dishoeck, E. F., Alcala, J. M., Myers, P. C., Stapelfeldt, K. R., Huard, T. L., Allen, L. E., Harvey, P. M., van Kempen, T., Blake, G. A., Koerner, D. W., Mundy, L. G., & Padgett, D. L. 2009, The Spitzer c2d Legacy Results: Star-Formation Rates and Efficiencies; Evolution and Lifetimes, ApJS, 181, 321E

Greene, T. P., Wilking, B. A., André, P., Young, E. T., & Lada, C. J. 1994, Further Mid-Infrared Study of the Rho Ophiuchi Cloud Young Stellar Population: Luminosities and Masses of Pre-Main-Sequence Stars, ApJ, 434, 614

Ivezic, Z., Neukova, M., & Elitzur, M. 1999, User Manual for DUSTY, astro-ph/104751

Jeong, W.-S., Nakagwa, T., Yamamura, I., et al. 2007, The Far-Infrared properties of Spatially Resolved AKARI Observations, PASJ, 59, 429

Kawada, M., Baba, H., Barthel, P. D., et al. 2007, The Far-Infrared Surveyor (FIS) for AKARI, PASJ 59S, 389K

Lada, C. J., & Wilking, B. A. 1984, The Nature of the Embedded Population in the Rho Ophiuchi Dark Cloud - Mid-Infrared Observations, ApJ, 287, 610L

Lada, C. J. 1987, Star Formation - From OB Associations to Protostars, IAUS, 115, 1L

Lee, J.-E., Bergin, E. A., & Evans, N. J. II, 2004, Evolution of Chemistry and Molecular Line Profiles during Protostellar Collapse, ApJ, 617, 360

Myers, P. C., & Lada, E. F. 1993, Bolometric Temperatures of Young Stellar Objects, ApJ, 413, 47M

Neugebauer, G., Habing, H. J., van Duinen, R., et al. 1984, The Infrared Astronomical Satellite (IRAS) Mission, ApJ, 278, 1N

Ossenkopf, V., & Henning, T. 1994, Dust opacities for protostellar cores, A&A, 291, 943O

Shirley, Y. L., Evans, N. J. II, & Rawlings, J. M. C. 2002, Tracing the Mass during Low-Mass Star Formation. III. Models of the Submillimeter Dust Continuum Emission from Class 0 Protostars, ApJ, 575, 337S

Shu, F. H. 1977, Self-Similar Collapse of Isothermal Spheres and Star Formation, ApJ, 214, 488S

Skrutskie, M. F., Cutri, R. M., Stiening, R., et al. 2006, The Two Micron All Sky Survey (2MASS), AJ, 131, 1163

Wheelock, S. L., Gautier, T. N., Chillemi, J., Kester, D., McCallon, H., Oken, C., White, J., Gregorich, D., Boulanger, F., & Good, J. 1994, IRAS Sky Survey Altas : Explanatory Supplement, STIN, 9522539W

White, R. J., Greene, T. P., Doppmann, G. W., Covey, K. R., & Hillenbrand, L. A. 2007, Stellar Properties of Embedded Protostars, Protostars and Planets V, 117

Wilking, B. A., Lada, C. J., & Young, E. T. 1989, IRAS Observations of Rho Ophiuchi Infrared Cluster-Spectral Energy Distributions and Luminosity Function, ApJ, 340, 823

Yamamura, I., Makiuti, S., Ikeda, N., Fukuda, Y., Oyabu, S., Koga, T., & White, G. J. 2010, AKARI/FIS All-Sky Survey Bright Source Catalogue Version 1.0 Release Note

Young, C. H., Shirley, Y. L., Evans, N. J. II, & Rawlings, J. M. C. 2003, Tracing the Mass during Low-Mass Star Formation, IV. Observations and Modeling of the Submillimiter Continuum Emission from Class I Protostars, ApJS, 145, 111

Young, C. H., & Evans, N. J. II, 2005, Evolutionary Signatures in the Formation of Low-Mass Protostars, ApJ, 627, 293Y